Mitigating Incidence Angle Effects in Airborne SAR Time-Series Crop Classification: Integrating Transfer Learning and Variational Mode Decomposition

Xingli Qin, Lingli Zhao, *Member, IEEE*, Jie Yang, Pingxiang Li, Hongwei Zeng, Miao Zhang, and Kaimin Sun, *Member, IEEE*

***Abstract*—This study introduces a novel approach to improve crop classification accuracy in airborne synthetic aperture radar (SAR) time-series imagery, focusing on overcoming the challenges posed by the incidence angle effect. The approach aims to innovate the integration of transfer learning and variational mode decomposition techniques. Transfer learning effectively addresses disparities in data distribution caused by varying incidence angles encountered in airborne SAR. Variational mode decomposition extracts robust temporal features, significantly reducing sensitivity to incidence angle variations. The approach is further enhanced by incorporating incidence angle information into the transfer learning model's training phase. The experimental results demonstrate the effectiveness of the method, which, under comparable sample conditions, achieves a remarkable improvement in accuracy (Kappa +25.05%) compared with the conventional methods. This improvement is particularly notable for crops, such as oats and soybeans, which are considerably influenced by the incidence angle effect, with Kappa increases of 27.92% and 39.30%, respectively. This study not only develops an effective strategy for crop classification in the context of airborne SAR imagery but also provides references for the effective use of new technologies from various fields in the field of remote sensing application.**

***Index Terms*—Airborne synthetic aperture radar (SAR), crop classification, incidence angle effect, time-series imagery, transfer learning, variational mode decomposition (VMD).**

Manuscript received 20 May 2024; revised 16 July 2024; accepted 1 August 2024. Date of publication 5 August 2024; date of current version 26 August 2024. This work was supported in part by the National Natural Science Foundation of China under Grant 61971318 and Grant U2033216, in part by the Natural Science Foundation of Hubei Province under Grant 2022CFB193, in part by the Agricultural Remote Sensing Innovation Team Project of AIRCAS under Grant E33D0201-6, and in part by the Youth Innovation Promotion Association of Chinese Academy of Sciences. *(Corresponding author: Lingli Zhao.)*

Xingli Qin and Miao Zhang are with the Key Laboratory of Remote Sensing and Digital Earth, Aerospace Information Research Institute, Chinese Academy of Sciences, Beijing 100101, China (e-mail: qinxl@aircas.ac.cn; zhangmiao@aircas.ac.cn).

Lingli Zhao is with the School of Remote Sensing and Information Engineering, Wuhan University, Wuhan 430079, China (e-mail: zhaolingli@whu.edu.cn).

Jie Yang, Pingxiang Li, and Kaimin Sun are with the State Key Laboratory of Information Engineering in Surveying, Mapping, and Remote Sensing, Wuhan University, Wuhan 430079, China (e-mail: yangj@whu.edu.cn; pxli@whu.edu.cn; kaiminsun@163.com).

Hongwei Zeng is with the Key Laboratory of Remote Sensing and Digital Earth, Aerospace Information Research Institute, Chinese Academy of Sciences, Beijing 100101, China, and also with the College of Resources and Environment, University of Chinese Academy of Sciences, Beijing 100049, China (e-mail: zenghw@aircas.ac.cn).

Digital Object Identifier 10.1109/JSTARS.2024.3438762

I. Introduction

IN THE context of global change, securing food has become increasingly critical [1]. Precise agricultural monitoring is an indispensable tool in achieving this goal, with the accurate crop distribution mapping being an important component of this endeavor [2]. The accurate mapping does not only involve obtaining a granular view of the agricultural landscape but also significantly contributes to strategies for maintaining food security [3], [4]. Policymakers and agricultural stakeholders are better equipped to make decisions that strengthen the resilience of food systems in the face of emerging challenges by providing crucial data [5], [6].

In recent years, synthetic aperture radar (SAR) technology has garnered considerable attention as an important tool in agricultural remote sensing [7], [8], [9]. Airborne SAR, in particular, with its high-frequency, flexible imaging capabilities, and superior spatial resolution has established itself as an invaluable supplementary asset for crop monitoring [10]. Its ability to provide timely data crucial for crop growth models, yield predictions, and disaster assessments is unparalleled, largely due to the sensitivity of the microwave signal to the dielectric and geometrical properties of crops. It captures backscattering coefficients, which serve as the composite reflection of land-cover type, terrain slope, surface roughness, local incidence angle, and dielectric constant, offering a multifaceted view of the agricultural landscape [11], [12]. However, despite its immense potential, airborne SAR faces significant challenges in crop distribution mapping, most notably the incidence angle effect. This effect is evident not only in airborne SAR but also in other SAR platforms, such as spaceborne systems. The incidence angle effect primarily stems from the side-looking imaging geometry of SAR systems and the spatial variation of target scattering properties. Therefore, it is closely related to radar operating parameters (such as frequency and polarization) and imaging modes. This phenomenon, exacerbated by the lower flying altitude of airborne platforms and the side-looking nature of SAR sensors, results in a wide range of incidence angle variations, thereby affecting the consistency of backscatter information [13], [14]. Such an effect complicates the analysis and accurate interpretation of land-cover types in SAR imagery, particularly in the fine classification of crops, where it can substantially impact classification accuracy.

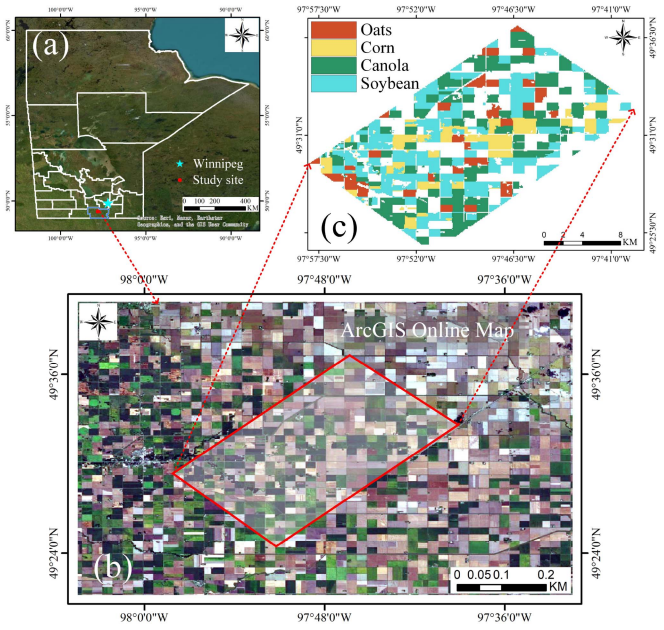

Fig. 1. Overview of the study area. (a) Location of the study area. (b) Overview of the study area in ArcGIS online map. (c) Reference map of crop distribution in the study area.

In response to the incidence angle effect, researchers have adopted various strategies to mitigate its influence. A common tactic is to exclude image areas with excessively large incidence angles to reduce their overall impact by simply ignoring the most affected areas [15], [16], [17]. Alternatively, some studies have focused on specific incidence angle correction techniques [13], [14], [18], [19], often based on intricate SAR backscatter models, to mathematically compensate for the effect of incidence angles. These methods are often proposed based on the physical scattering characteristics of specific research objects. For example, excluding large incidence angle regions is conducive to obtaining stable scattering information for rice (short) and corn (tall). Therefore, these methods have clear physical-driven characteristics, but with certain limitations. Excluding areas with large incidence angles can effectively avoid the incidence angle effect. However, it results in a significant loss of image information, a tradeoff that is often untenable. Moreover, correction techniques, although potentially effective under certain conditions, generally lack universality because of the complex and diverse nature of agricultural environments. Factors, such as crop type, growth stage, and soil conditions, can introduce variations in SAR backscatter, complicating the development of a one-size-fits-all correction approach.

To address these challenges and fully utilize the potential of airborne SAR data, an innovative approach is introduced. Contrary to previous studies that focus on the physical properties of research objects, the traditional methods have difficulties in dealing with the varying scattering behavior under complex agricultural landscapes; thus, data-driven classification strategies are explored. We acknowledge the limitations of standard classification methods, which face difficulties with data recorded at varying incidence angles. Therefore, we have incorporated transfer learning [20], [21], a machine learning strategy that effectively bridges disparities in data distributions between source and target domains. By using transfer learning, our model can apply knowledge gained from one incidence angle to data from another, reducing the variability caused by the incidence angle effect. Furthermore, we have incorporated innovative variational mode decomposition (VMD) methods [22], [23] from the field of signal processing for feature extraction. We can derive robust features that are less susceptible to changes in incidence angles by capturing the dynamic growth patterns and cyclical shifts of crops.

Our research is dedicated to the integration of advanced technologies, such as transfer learning and VMD, to develop a robust and accurate framework for crop classification using airborne SAR data, specifically addressing the incidence angle effect in airborne SAR crop classification. The main innovations of this study include the following:

1) Introducing transfer learning into airborne SAR crop classification and exploring strategies for guiding the transfer learning process by incorporating incidence angle information;
2) Innovatively applying VMD in the field of crop classification to extract robust temporal features;
3) Investigating the mechanism of polarization information in mitigating the incidence angle effect and improving classification performance.

The rest of this article is organized as follows. In Section II, we present the data used in our study and analyze the impact of incidence angle effects on the data. Then, in Section III, the proposed method is introduced in detail. The experimental results are analyzed in Section IV. The effectiveness of our method in mitigating the impact of incidence angle effects and the ability of VMD to extract robust features are comprehensively discussed in Section V. Finally, Section VI concludes this article.

II. Data

A. Overview of Study Area and Experimental Data

The study area is located near the city of Winnipeg in Manitoba, Canada, as shown in Fig. 1(a). Its location on the ArcGIS online map is depicted in Fig. 1(b). Four types of crops were selected for the crop classification experiment, including oats, corn, canola, and soybean. The distribution reference map of the crops is presented in Fig. 1(c); it was established in accordance with the land-cover classification map produced by the NASA National Snow and Ice Data Center Distributed Active Archive Center [24].

The data used in this study were sourced from the uninhabited aerial vehicle synthetic aperture radar (UAVSAR) imagery obtained from "The Soil Moisture Active Passive Validation Experiment 2012" (SMAPVEX12) [16], [24]. SMAPVEX12 was conducted to support the development, enhancement, and testing of the SMAP soil moisture retrieval algorithm. The experiment lasted for 43 days (7–19 June 2012), during which UAVSAR imaged the area for 13 days [16]. This study utilized 12 scenes of UAVSAR imagery, with their corresponding Pauli RGB images, as shown in Fig. 2(a)–(l). The data were captured in the *L*-band frequency (1.26 GHz) with a left-look direction. The

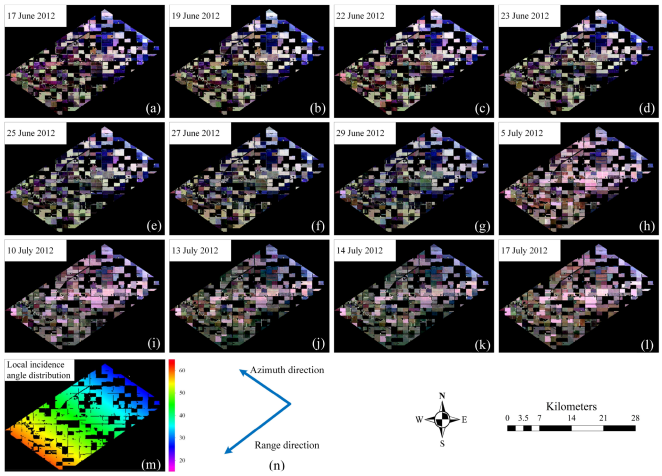

Fig. 2. Overview of the experimental data. (a)–(l) Pauli RGB images. (m) Local incidence angle distribution. (n) Azimuth and range direction of the images.

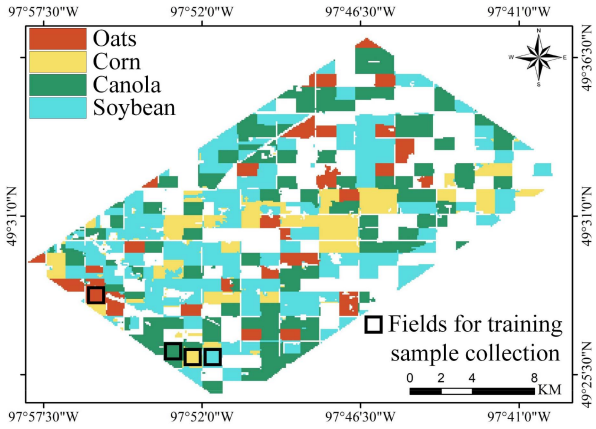

Fig. 3. Distribution of training samples.

acquired single-look complex data have a spatial resolution of 0.6 m in the azimuth direction and 1.67 m in the range direction.

Consistent with the previous study [10], these images underwent multiview processing (with 15 views in range and 60 views in azimuth) and were downsampled by a factor of three, covering a ground range of 22 680 m × 24 566 m. The local incidence angle size corresponding to each pixel on the image is shown in Fig. 2(m), with the minimum local incidence angle being 21.2° (near range of the image) and the maximum being 64.3° (far range of the image). The local incidence angle is defined as the angle between the radar line-of-sight and the surface normal vector [25].

The Pauli RGB images evidently illustrate that the backscatter characteristics of the same type of crop at near and far ranges are significantly different. Factors influencing the backscatter coefficient of crops in SAR images include terrain slope, crop geometry, soil moisture content, and incidence angle. The growth conditions of the same types of crops are assumed to be consistent, given the small area of the region. In addition, the terrain slope of the area ranges between 0% and 2%, and the primary soil types are loam and clay. The moisture content differences between these soil types are minimal [16], suggesting that the impacts of terrain slope and soil moisture content are also minimal. Consequently, the significant incidence angle effect caused by the large variation in image incidence angles is the primary reason for the pronounced differences in backscatter characteristics of the same crop type at near and far ranges [10]. Therefore, in Section II-B, we provide a detailed analysis of the effect of angle of incidence differences on crop distinguishability. Moreover, given the flat terrain of the area, the local incidence angle of a pixel is assumed to be equivalent to its incidence angle. For ease of description, they are collectively referred to as the incidence angle in the following content.

Several studies [26], [27], [28] have shown that the cross-polarization channel (HV) in SAR time-series imagery is more effective for crop differentiation than the horizontal (HH) and vertical (VV) channels. Consequently, this research utilizes only the backscatter coefficient (S_{HV}) from the cross-polarization channel for crop classification. This approach not only streamlines the analysis but also offers a benchmark for other single- or dual-polarization crop mappings. Each sample S_i time-series curve is derived from its S_{HV} across all images, as shown in the following equation:

$$S_i = \left\{S_{HV}^{t_1}, S_{HV}^{t_2}, \ldots, S_{HV}^{t_n}\right\} \tag{1}$$

where t is the time of observation, and n is the number of observations within the time series.

B. Data Analysis

1) Data Distribution in H-Alpha Space: The synthesis of time-series data and machine learning classifiers has emerged as a prevalent and efficacious strategy for crop classification [29], [30]. This methodology necessitates a substantial quantity of training samples from diverse crop types, enabling the machine learning classifier to learn with high efficacy. However, data distributions across different regions exhibit substantial variability, owing to the incidence angle effects.

Contrary to the globally random sampling method typically employed in image analysis, a sample collection method more congruent with realistic application scenarios is explored in this study. We have methodically collected and labeled samples from a localized region (see Fig. 3), subsequently utilizing these samples to train a classifier aimed at crop classification within the image. For each crop type, 100 samples were meticulously gathered. The training set is characterized by samples with an incidence angle range of 62.3°–64.2°, with an average of 63.4°. The remaining pixels within the image were designated as the test set.

To elucidate the complexity of land object distribution affected by the incidence angle effect, we have delineated the distribution of various land object elements and the training samples on the H-Alpha plane (see Fig. 4) using the average of the C3 matrices derived from the 12 time-series images.

The H-Alpha plane, a pivotal feature space in polarimetric SAR data, is instrumental in classifying the different types of surfaces or targets. It delineates the entropy (H) and alpha angle

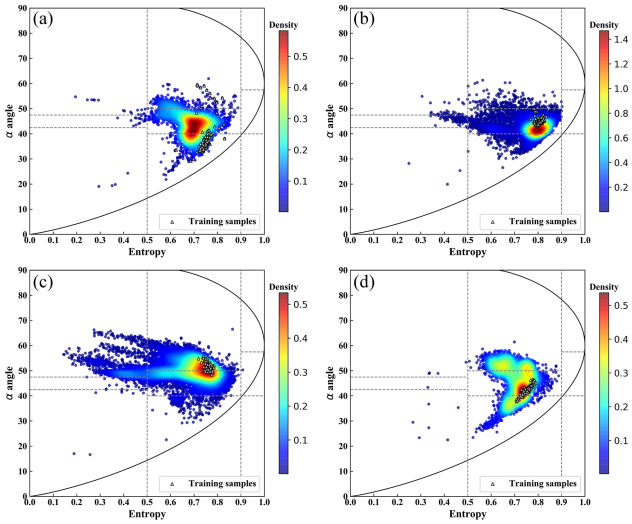

Fig. 4. Distribution of samples on the H-Alpha plane. (a) Oats. (b) Canola. (c) Soybean. (d) Corn.

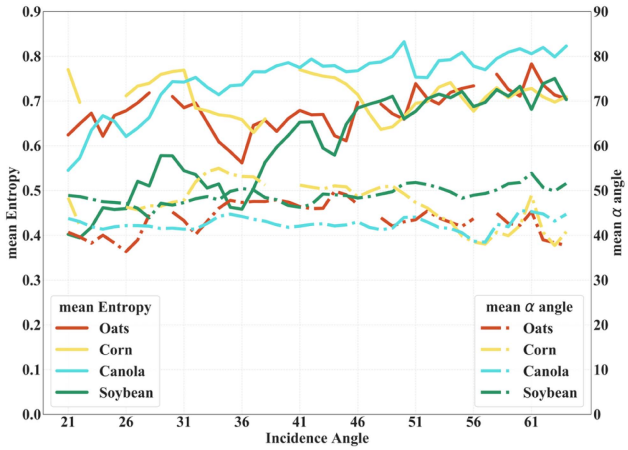

Fig. 5. Mean entropy and mean alpha angle of different crop types as a function of incidence angle.

(α) of the radar return. These parameters are intrinsically linked to the randomness of the scattering process and the predominant scattering mechanism. In this context, entropy (H) quantifies the randomness of the scattering process, where lower values signify more deterministic scattering, and higher values indicate a more random nature. Conversely, the alpha angle (α) pertains to the type of scattering mechanism, with lower angles typically reflective of surface scattering, and higher angles indicative of volume or multiple scattering.

The pixel distribution of oats is defined by a moderate to high entropy range, with entropy values generally spanning from 0.5 to 0.9 and alpha angles from 30° to 60°. The positioning of the high-density, red area indicates that oats are primarily influenced by multiple scattering mechanisms, a characteristic of vegetative structures with considerable volume scattering.

Canola shows a moderately high entropy distribution, with the red high-density area covering entropy values from roughly 0.4 to 0.9 and alpha angles clustering between 30° and 60°. The spread within the red area for canola points to a diverse range of scattering behavior, reflecting different canopy densities or stages of growth. The extent of this region underscores the complexity of canola's physical attributes because they interact with SAR signals.

The soybean pixels display a broad distribution in the entropy and alpha angle, with the red high-density region indicating the most common scattering properties. The expansive nature of this region, covering a wide range of entropy values and alpha angles, suggests significant variability in the soybean fields' scattering mechanisms. This variation could be attributed to differences in growth stages, plant density, or soil moisture conditions, influencing the SAR signal's response.

Corn pixels are characterized by a more concentrated distribution in a higher entropy region, specifically with the red high-density area showing entropy values predominantly above 0.7 and alpha angles around 40°–60°. The concentrated nature of corn's red area reflects a consistent scattering behavior, likely due to its uniform growth pattern and dense canopy structure that results in pronounced volume scattering.

Ideally, distinct clusters in the H-Alpha space would represent each crop type, streamlining the classification process. However, the observed distributions indicate some overlap degrees, especially between oats and canola, sharing a high-density region with entropy values from 0.4 to 0.8 and alpha angles from 30° to 60°. This shared space complicates the discriminability between the two crops. Soybeans, with their wide-ranging high-density area across entropy and alpha angle values, exhibit a diverse scattering behavior, further challenging the classification. Conversely, corn is characterized by a compact and higher entropy cluster. However, its alpha angle proximity to other crops may still lead to classification difficulties due to the overlapping regions.

In addition, the density plots suggest that the training samples, represented by triangles and limited to an incidence angle range of 62.3°–64.2°, do not cover the entire range of scattering behavior observed in the entire image. This restricted sample set may lead to inaccuracies in classification, particularly when applied to areas with incidence angles that differ significantly from those of the training data. This challenge is particularly relevant in airborne SAR imagery, characterized by varying incidence angles that can lead to data distribution inconsistencies. As a result, it affects the dependability of classification outcomes.

We have generated an additional figure (see Fig. 5) that depicts the variation of mean entropy and mean alpha angle as a function of incidence angle for the four crop types, further illustrating the impact of the incidence angle effect on the polarimetric scattering properties of different crop types.

As shown in Fig. 5, the mean entropy and mean alpha angle of all four crop types exhibit significant variations with the incidence angle. The mean entropy generally shows an increasing trend as the incidence angle increases from approximately 21° to 61°, whereas the mean alpha angle demonstrates a fluctuating trend for most crop types. The variation patterns of mean entropy and mean alpha angle differ among crop types, suggesting that the incidence angle effect impacts the polarimetric scattering

properties of different crops in distinct approaches. The separability of different crop types in the H-Alpha space also varies with the incidence angle. The separability of crops decreases as the incidence angle increases.

These observations provide compelling evidence that the incidence angle effect significantly influences the polarimetric scattering characteristics of crops, thereby affecting their separability and classification performance.

2) Analysis of Incidence Angle Variability on Classification Accuracy: Classification accuracy in image-based models depends heavily on the consistency of distribution between the training and test datasets. This condition is salient in the domain of SAR imagery, where the natural variance in incidence angles can significantly challenge the classifier's generalizability. To investigate the effect of incidence angle variability on classification accuracy, we conducted the following analytical procedure using the UAVSAR dataset.

1) The pixels on the image, forming the sample set U, are uniformly divided into ten sample subsets along the range direction: $\{U_1, U_2, \ldots, U_{10}\}$.
2) Each sample subset is randomly divided into a training set (20%) and a test set (80%), resulting in ten training sets $\{U_1^{\text{tr}}, U_2^{\text{tr}}, \ldots, U_{10}^{\text{tr}}\}$ and ten test sets $\{U_1^{\text{te}}, U_2^{\text{te}}, \ldots, U_{10}^{\text{te}}\}$.
3) For each training set U_i^{tr}, a classifier is trained using only that set. Then, the trained classifier is used to classify all test sets $\{U_1^{\text{te}}, U_2^{\text{te}}, \ldots, U_{10}^{\text{te}}\}$, yielding classification accuracy $P_i = \{P_i^1, P_i^2, \ldots, P_i^{10}\}$ for each test set.
4) A total of 100 classification accuracy sets can be derived from the ten training sets: $\langle\{P_1^1, P_1^2, \ldots, P_1^{10}\}, \{P_2^1, P_2^2, \ldots, P_2^{10}\}, \ldots, \{P_{10}^1, P_{10}^2, \ldots, P_{10}^{10}\}\rangle$, with each set corresponding to a training set and a test set.

Steps (1) and (2) are repeated ten times, and the average value from these ten experiments is considered the result for each set of classification accuracy. The deep forest (DF) [31] model is used as the classifier, and the Kappa coefficient is used to measure the classification accuracy. All values of a sample S_i time-series curve are used as the features.

Fig. 6 presents a matrix heatmap of the 100 sets of classification accuracies. The x-axis delineates the average incidence angle magnitude for the test sets, while the y-axis corresponds to the average incidence angle magnitude for the training sets. Each cell within the matrix epitomizes a unique combination of training and test sets, characterized by their respective average incidence angles. The matrix's secondary diagonal, extending from the bottom left to the top right, represents pairs with equivalent average incidence angles.

The pattern within the matrix is clear: cells near the secondary diagonal have higher Kappa coefficient values, indicating better classification accuracy. This condition highlights the need for the alignment of incidence angles between the training and test sets to achieve optimal classifier performance. Conversely, a difference in average incidence angles between the datasets, indicated by cells further from the secondary diagonal, is associated with a decrease in classification accuracy.

The heatmap supports the hypothesis that incidence angle congruence is crucial for reliable SAR image-based crop classification. The color gradation on the heatmap, from green to red, reflects the decrease in classification accuracy as incidence angle differences increase. This trend is particularly noticeable when moving from cells adjacent to the diagonal to those at the matrix's far reaches. Cells with Kappa coefficients nearing 0.9 exhibit the highest level of accuracy, which is concentrated around the secondary diagonal. On the contrary, the lowest level of accuracy, with values as low as 0.15, is found at the peripheries of the matrix. This result confirms the following phenomenon: as the incidence angle difference between the training and test sets increases, the classification accuracy decreases.

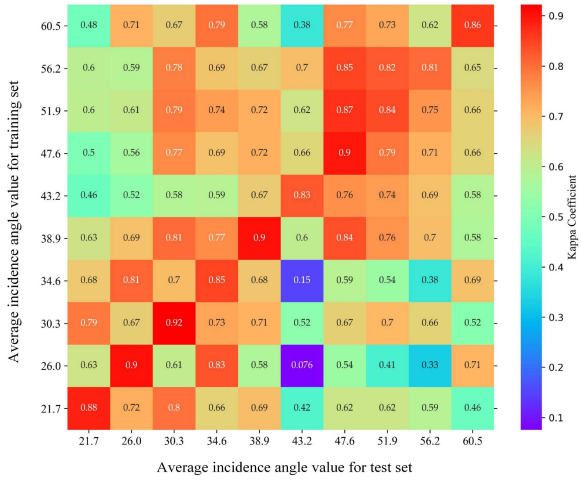

Fig. 6. Correlation between incidence angle differences in training and test sets and classification accuracy.

The findings from this analysis underscore the substantial impact of the incidence angle effect on crop classification performance. The observed relationship between incidence angle differences and classification accuracy can be attributed to the changes in the scattering mechanisms of crops induced by varying incidence angles. The interaction between the SAR signal and crop canopy structures is altered as the incidence angle changes, leading to modifications in the polarimetric scattering properties of crops. These changes, in turn, affect the separability of crop types in the feature space and, consequently, degrade the classification performance.

The insights gained from this analysis are crucial for understanding the challenges posed by the incidence angle effect in SAR-based crop classification and highlight the necessity of developing robust methods to mitigate its impact. This section provides a strong foundation for the proposed approach in this study by establishing a clear link between incidence angle differences and classification accuracy. This approach integrates transfer learning and VMD techniques to enhance the adaptability and robustness of crop classifiers in the presence of incidence angle variations.

III. Method

A. Overview of the Proposed Crop Classification Method

The data analysis results confirm that the incidence angle effect is a crucial factor affecting the accuracy of crop-type

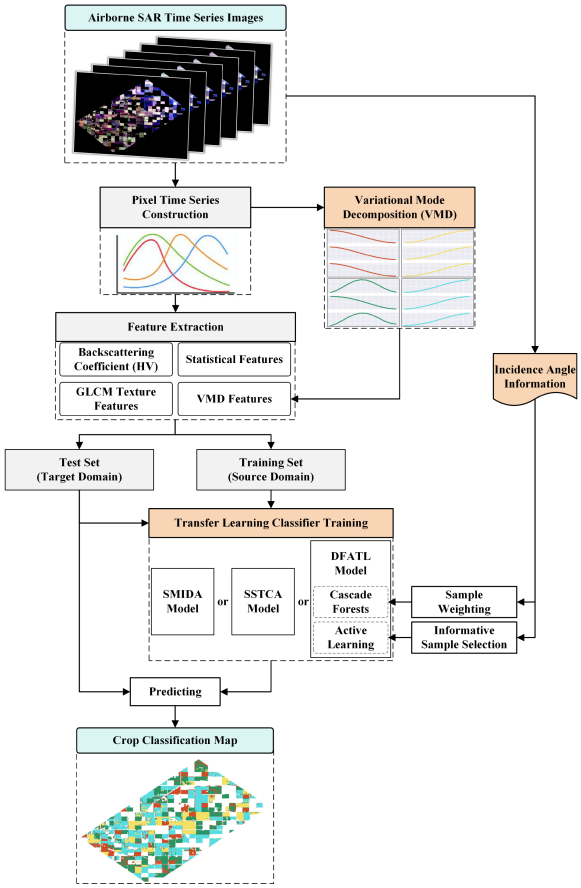

Fig. 7. Flowchart of the proposed method.

classification in airborne SAR imagery. It primarily causes inconsistencies in data distribution between the training and test sets. In addition, it renders conventional horizontal and vertical polarization (HV) time-series curves less effective at representing the differences between various crops. These factors significantly degrade the model's predictive performance [32].

To address these challenges, our approach leverages the transfer learning technique. Transfer learning is designed to adapt the learned knowledge from one domain (source) and apply it to another (target) effectively. This method mitigates the impact of the data distribution differences attributed to the incidence angle effect. In terms of feature representation, we extract a richer set of features from the original time-series data, augmenting the backscattering coefficients with statistical and textural features, as well as those derived from VMD, to improve their representational capability.

We also explore the feasibility and effectiveness of incorporating incidence angle information as critical reference data into the model training process. This approach aims to refine the classifier's performance by enabling the model to more accurately capture the characteristics of the data encountered in actual SAR image classification tasks.

The proposed procedure is illustrated in Fig. 7. The workflow commences with the construction of pixel time series from time-series images, followed by a VMD decomposition to enrich the feature set. The enhanced features undergo extraction, covering backscattering coefficients, statistical features, GLCM texture features, and VMD features. Then, they are used to train transfer learning classifier in which the DF-based active transfer learning (DFATL) method is further bolstered by active learning mechanisms, such as cascade forests and informative sample selection, with incidence angle information being a critical factor in sample weighting. The trained classifier is subsequently tasked with predicting the classes on the test set, culminating in the generation of a comprehensive crop classification map.

B. Time-Series Feature Extraction

As mentioned in Section II-A, the backscatter coefficient (S_{HV}) of the cross-polarization channel (HV) is used to form the time-series curve for crop classification. In addition, the S_{HV} time series is referred to as the sample's original features for simplicity.

When using the original features for classifier training and considering these time-series features as isolated attributes, altering the order of feature arrangement does not affect the classifier's performance. Thus, the sequential relationship of the original features in the temporal dimension is not exploited. However, we believe that the arrangement of the original features in the temporal dimension encapsulates the crop's changing trend over time. This technique is highly effective in distinguishing different crop types. Therefore, to harness this information embedded in the time series for classifier training, feature extraction is conducted using the original features.

1) VMD Features: Crop time-series curves fluctuate due to two primary factors: crop growth trends and soil moisture changes. While the former reflects the crop's growth pattern, the latter introduces significant variability, often influenced by events, such as rainfall or irrigation [33], [34]. By isolating curve variations attributed to crop growth from those caused by soil moisture changes, the time-series curve can more effectively capture crop dynamics, enhancing crop-type differentiation.

Decomposing multicomponent signals into individual components is often essential in signal processing for modal parameter identification [35], [36]. Leveraging this concept, we introduce the VMD algorithm for our analysis [22].

The core procedure of VMD is depicted in Fig. 8. The VMD algorithm assumes a signal that comprises overlaid subsignals with distinct frequencies. It aims to decompose the signal into these frequency-specific components. The algorithm adaptively partitions the signal's frequency domain by iteratively finding the optimal solution of the variational model, determining each component's center frequency and bandwidth. Within VMD, the intrinsic-mode function (IMF) is viewed as an amplitude-modulated–frequency-modulated signal. The algorithm's objective is to break down the original signal into a set number of IMF components by addressing a constrained variational problem.

The algorithm for VMD can be described as follows:

Initialization:

The VMD algorithm begins with an initial setting of the mode functions u_k, associated center frequencies ω_k, the Lagrange multiplier λ, and iteration count $n = 0$.

Iteration:

(1) The iteration index n is incremented by 1.

(2) A mode index k is initialized to 1.

Mode Update:

(3) For each mode k, the mode function u_k is updated by solving the following optimization problem, aimed at minimizing the bandwidth of the mode around its center frequency ω_k, as follows:

$$u_k^{n+1} = \arg\min_{u^k} L\left(\{u_{i<k}^{n+1}\}, \{u_{i\geq k}^{n}\}, \{\omega_i^n\}, \lambda^n\right) \tag{2}$$

This process involves the estimation of the mode with the current estimate of its center frequency while fixing the other modes and frequencies.

Convergence Check for Modes:

(4) The mode index k is incremented, and a check is performed to determine if all modes have been updated in this iteration.

(5) Otherwise, the **algorithm** returns to step 3 or resets k to 1 and proceeds to update the center frequencies.

Frequency Update:

(6) For each mode k, the center frequency ω_k is updated by solving a similar optimization problem to minimize the bandwidth, as follows:

$$\omega_k^{n+1} = \arg\min_{\omega_k} L\left(\left\{u_i^{n+1}\right\}, \left\{\omega_{i<k}^{n+1}\right\}, \left\{\omega_{i\geq k}^{n}\right\}, \lambda^n\right). \tag{3}$$

Convergence Check for Frequencies:

(7) After updating all frequencies, a convergence check is performed to determine whether the difference between the current and previous mode functions is smaller than a predefined threshold ε.

Lagrange Multiplier Update:

(8) If convergence is not achieved, then the Lagrange multiplier λ is updated using the residue of the original signal and the sum of all modes, as follows:

$$\lambda^{n+1} = \lambda^n + \tau\left(f - \sum_k u_k^{n+1}\right) \tag{4}$$

where τ is the step size of the Lagrange multiplier update.

Termination:

(9) The convergence check is performed again, this time including the criterion based on the squared L^2 norm of the difference between mode functions from successive iterations normalized by the norm of the previous mode function.

(10) When the convergence criterion is satisfied, the algorithm is terminated, and the resulting modes, known as IMFs, are output.

Output:

(11) The final step is to output the K IMFs that represent the decomposed signal.

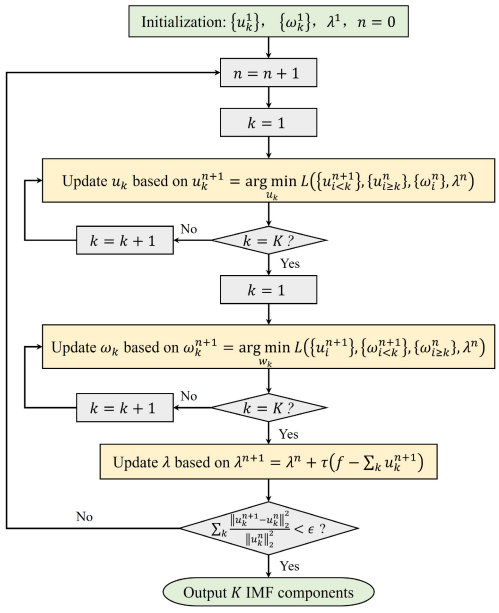

Fig. 8. Flowchart for VMD algorithm (adapted from [37]).

Dragomiretskiy and Zosso [22] present a more detailed discussion of the VMD algorithm.

In this study, we effectively decomposed the HV time-series data into two distinct components by setting the mode number for VMD to 2. The first component captures information related to variations in soil moisture; it is significantly influenced by precipitation events, thereby exhibiting a degree of randomness in its temporal evolution. However, the second component contains information that is specifically related to the crop growth cycle, making it particularly useful for crop classification. Therefore, we extract this second component as a key feature set for subsequent model training and classification tasks. In this experimental analysis and discussion, we thoroughly assess the effectiveness of VMD decomposition in mitigating incidence angle effects in crop classification and explore its potential applications in agricultural remote sensing.

2) Gray-Level Co-Occurrence Matrix (GLCM) Texture Features: The enhancement of image resolution allows for a clearer representation of detailed information on the image. The rich detail information of similar pixels in adjacent areas forms the unique texture features of the object. Texture features are patterns and characteristics formed by the frequent repetition of small objects on an image. They are a comprehensive reflection of the size, shape, shadow, and color of a large number of individuals, describing the spatial variation characteristics of pixel brightness. We believe that texture features can suppress the influence of the incidence angle effect to some extent.

The GLCM is a widely used effective image texture feature, established to estimate the second-order joint conditional probability density of the image. GLCM describes the occurrence probability of a pair of pixels with gray levels *i* and *j*, separated by a pixel distance d in the θ-direction. A total of 14 texture features can be derived using GLCM [38]. However, only three GLCM features, namely, homogeneity, contrast, and entropy are

TABLE I
FEATURES USED FOR CLASSIFICATION

Feature name	Feature values	Dimensions	Denoted as
Original feature	$\{S_{HV}^{t_1}, S_{HV}^{t_2}, \ldots, S_{HV}^{t_n}\}$	12	F1
GLCM texture feature	Homogeneity, contrast, and entropy from 12 images	36	F2
Statistical feature	Standard deviation, interquartile range (upper quartile − lower quartile), upper quartile, lower quartile, maximum value, minimum value, mean, and median of original features	8	
VMD feature	The second component from VMD decomposition	12	F3

used to avoid excessive feature dimensions because each sample can derive a set of GLCM features from each time phase image. In this study, 12 images were used; thus, each sample can obtain a 36-D (12×3) GLCM texture feature.

3) Statistical Features of Time-Series Features: We also employed feature extraction using statistical methods. Information collected on different dates within the same year or over consecutive years can be statistically summarized into various indicators. These indicators can effectively differentiate land-cover types [39]. We extracted the following 8-D features: standard deviation, interquartile range (upper quartile–lower quartile), upper quartile, lower quartile, maximum value, minimum value, mean, and median.

We categorized the features into three groups for the subsequent experiments to evaluate the efficacy of temporal sequence features developed for this research. F1 represents the original features derived directly from SAR data; F2 encompasses the traditional features, which include statistical attributes of the temporal curves and GLCM texture features; and F3 comprises the innovative-mode decomposition features, which are novel to this study's approach. These delineated feature sets serve as the foundational elements for the detailed crop classification, as presented in Table I.

C. Transfer Learning

Transfer learning methods, which often serve as machine learning classifiers, use samples from a source domain to train models that can classify unlabeled samples in a target domain [40], [41]. This process considers classification as a labeling exercise for the target-domain's unlabeled samples, positioning it within the broader context of image classification tasks.

When the training set (source domain) and the test set (target domain) have the same data distribution, the performance of the transfer learning model may unnecessarily surpass that of the conventional machine learning classifiers. However, when data distribution difference exists between the training and test sets, conventional machine learning classifiers often experience a significant performance decline, whereas transfer learning models can still accurately classify the test set [21]. Hence, when directly applying transfer learning models to image classification tasks, these models are referred to as transfer learning classifiers.

In the scenario set (where the training set comes from the far end of the image, and the test set consists of other pixels of the image, as shown in Fig. 3), we introduce transfer learning classifiers to enhance the classification accuracy of the test set, thereby addressing the issue of reduced classification accuracy due to distribution differences between the training and test sets. We used two types of transfer learning classifiers in the experiments.

The first transfer learning classifier is the DFATL tailored for polarized SAR images. The existing research [42] indicates that this method boasts excellent performance and strong scalability. Therefore, we integrated the sample's incidence angle information into the model training process of this method to enhance its performance.

The second transfer learning classifier is semisupervised MIDA (SMIDA) [43], which is a semisupervised extension of the MIDA framework. Operating within the semisupervised paradigm, SMIDA harnesses labeled and unlabeled target-domain data, effectively mitigating the discrepancy between the training and test set distributions. This approach is particularly beneficial in our study scenario because it enhances classification accuracy where the training and test sets exhibit significant distributional differences, as depicted in our experimental setup. By judiciously utilizing the unlabeled data alongside the labeled examples, SMIDA contributes to a more robust and accurate model adaptation, aligning with the overarching goal of improving SAR image classification performance in this research.

The third transfer learning classifier is the semisupervised transfer component analysis (SSTCA) algorithm [44]. This method is a feature-based transfer learning approach. It requires the computation of domain distribution differences between the source-domain samples and target-domain samples and then seeks effective feature mappings using these distribution differences. The maximum mean discrepancy (MMD) [45] is used as the data distribution measurement. When applying SSTCA to image classification tasks, the following must be considered: a large number of target-domain samples in image classification tasks must be examined prior to MMD computation, which is time-consuming and requires substantial computer storage. If the sampled subset is not representative, then the accuracy of MMD computation is affected, thereby influencing the SSTCA performance to some extent.

In addition to the three transfer learning classifiers, the DF model is employed as a conventional machine learning classifier for crop classification. This approach aims to evaluate the performance improvement brought about by using transfer learning classifiers. This model has demonstrated highly reliable performance in many classification tasks [31].

D. Incorporating Incidence Angle Information

We attempted to incorporate incidence angle information into the DFATL model to enhance classification performance. The DFATL model is well regarded for its interpretability and adaptability, allowing straightforward modifications to integrate incidence angle data. The introduction of incidence angle information into the DFATL training process aids in the selection of informative target-domain samples and the

weighting of training samples by accounting for distribution differences between training and test sets attributable to varying incidence angles. This integration optimizes the model's effectiveness. The methodology for this adaptation is detailed in the following sections.

1) Selection of Informative Target-Domain Samples Using Incidence Angle Information: The DFATL model's training comprises two phases: growth and filtering. In the growth phase, active learning iteratively selects high-information samples from the target domain for manual labeling, considering sample uncertainty and diversity [46]. This study refines these measures in DFATL by incorporating incidence angle information.

First, the method of calculating sample uncertainty in DFATL was adjusted as follows.

1) The average incidence angle of all samples in the training set, denoted as Inc_{mean}, is calculated.
2) The absolute difference between the incidence angles of all samples $\{S_1, S_2, \ldots, S_n\}$ in the test set and Inc_{mean}, denoted as $\{D_1,\ D_2, \ldots, D_n\}$, is computed.
3) The maximum value from $\{D_1,\ D_2, \ldots, D_n\}$, denoted as $D_{\max}$, is determined.
4) During each iteration, the uncertainty of sample S_i is calculated as follows:

$$\bar{U}_i = U_i + \frac{D_i}{D_{\max}} \times \sigma \tag{5}$$

where U_i is the uncertainty of sample S_i calculated in DFATL using class prediction probabilities, $\bar{U}_i$ is the adjusted uncertainty of sample S_i, and σ is a tuning coefficient (set to 0.1 in the experiments).

This adjustment is premised on the idea that, for a training set from the far end, near-end test set pixels may be more informative. This approach identifies samples with high uncertainty and notable training set distribution differences. After isolating a high-uncertainty target-domain sample set (G_u), DFATL further extracts diverse samples, forming the final high-information sample set (G_{u+d}).

Second, the method of measuring sample diversity was adjusted in the first three cascade layers of the growth phase as follows.

1) The extracted G_u is evenly divided into *N* subsets based on their incidence angles.
2) $G_{u+d} = \emptyset$ is set.
3) The sample with the highest uncertainty from each subset is selected, resulting in *N* samples.
4) *N* samples are added to G_{u+d}.
5) Steps (3) and (4) are repeated until the number of samples in G_{u+d} satisfies the requirements.

This adjustment ensures that the samples from the three initial iterations are uniformly distributed across various incidence angle regions. This condition promotes model generalization during initialization, preventing overfitting from excessive far-end sample selection. Following the initial phase, the original DFATL sample diversity measurement is employed in subsequent layers.

TABLE II
EXPERIMENTAL SETUP

Number	Denoted as	Classifier	Use F1	Use F2	Use F3	Use incidence angle
1	DF + F1	Deep Forest	1	0	0	0
2	DF + F1 + F2	Deep Forest	1	1	0	0
3	DF + F1 + F3	Deep Forest	1	0	1	0
4	DF + F1 + F2 + F3	Deep Forest	1	1	1	0
5	SSTCA + F1	SSTCA	1	0	0	0
6	SSTCA+ F1 + F2	SSTCA	1	1	0	0
7	SSTCA+ F1 + F3	SSTCA	1	0	1	0
8	SSTCA+ F1 + F2 + F3	SSTCA	1	1	1	0
9	SSTCA + F1	SMIDA	1	0	0	0
10	SSTCA+ F1 + F2	SMIDA	1	1	0	0
11	SSTCA+ F1 + F3	SMIDA	1	0	1	0
12	SSTCA+ F1 + F2 + F3	SMIDA	1	1	1	0
13	DFATL + F1	DFTAL	1	0	0	0
14	DFATL + F1 + F2	DFATL	1	1	0	0
15	DFATL + F1 + F3	DFATL	1	0	1	0
16	DFATL + F1 + F2 + F3	DFATL	1	1	1	0
17	DFATL + F1 + Angle	DFTAL	1	0	0	1
18	DFATL + F1 + F2 + Angle	DFATL	1	1	0	1
19	DFATL + F1 + F3+ Angle	DFATL	1	0	1	1
20	DFATL + F1 + F2 + F3+ Angle	DFATL	1	1	1	1

2) Using Incidence Angle Information to Weigh Target-Domain Samples: The selected high-information target-domain samples with DFATL are manually labeled and merged with the original training set for subsequent cascade layer training. To expedite model fitting, samples from G_{u+d} with pronounced distribution differences from source-domain samples are assigned higher weights, influencing the model more significantly.

Given the link between incidence angle and data distribution differences and using the precalculated absolute differences between each sample's incidence angle and the training set's average incidence angle $\{D_1,\ D_2, \ldots, D_n\}$, the weight w_i of each high-information target-domain sample is determined as follows:

$$w_i = 1.0 + \frac{D_i}{D_{\max}} \times \delta, \tag{6}$$

where δ is a tuning coefficient, set to 10. Hence, during training, a labeled target-domain sample with a notably different incidence angle from the source-domain average receives a higher weight.

IV. RESULTS

A. Experimental Setup

An in-depth analysis of the proposed method's effectiveness was conducted through a set of 20 distinct configurations, which are meticulously detailed in Table II.

The primary objective of these experiments was to systematically analyze the following.

1) The differential impact of employing transfer learning models versus conventional machine learning approaches.
2) The effectiveness of integrating VMD for feature extraction in contrast to non-VMD feature sets.
3) The potential enhancement in classification performance through the incorporation of incidence angle information.

Each experiment was designed to test the classification models across various combinations of features and additional information.

1) *DF Experiments (1–4):* It serves as a control group using only traditional machine learning techniques. They progressively integrate different feature sets, providing a baseline for performance comparison.
2) *SSTCA and SMIDA Experiments (5–12):* Transfer learning with SSTCA and SMIDA classifiers is employed to ascertain the benefits of transfer learning in reducing the incidence angle effect. These experiments also systematically add VMD features (F3) to evaluate their contribution to model accuracy.
3) *DFATL Experiments (13–20):* The DFATL model is leveraged to test the efficacy of transfer learning specifically adapted to this domain. These experiments are further enhanced with the introduction of incidence angle information, denoted as "Angle" in the table, to determine its influence on classification performance.

The experiments can be categorized into four main comparative analyses.

1) *Feature analysis (F1, F2, F3):* Experiments 1–4, 5–8, 9–12, and 13–16 examine the incremental benefit of each feature set, providing insights into the significance of each type of feature in isolation and in combination.
2) *Transfer learning analysis (DF versus DFATL/SSTCA/SMIDA):* The advantage of transfer learning over traditional methods can be evaluated by comparing experiments 1–4 with 5–16.
3) *VMD feature analysis:* Comparisons within experiments 1–4, 5–8, versus 9–12, and 13–16 versus 17–20 assess the impact of VMD features on the classification outcome.
4) *Incidence angle analysis:* Finally, experiments 17–20 allow for the evaluation of the classification improvement when incidence angle information is incorporated into the transfer learning model.

Feature selection is denoted as follows: F1 represents the basic SAR image features, F2 encompasses the additional features derived from traditional feature extract methods, and F3 indicates the features extracted through VMD. The incidence angle information (denoted by "Angle") is a novel inclusion aimed at enhancing the model's contextual understanding of the SAR data.

In executing these experiments, we employed multiple evaluation metrics to comprehensively assess the classifier's performance. The Kappa coefficient was primarily used as it effectively evaluates the consistency of classification results and demonstrates good adaptability to class imbalance scenarios. The results derived from the Kappa coefficient are expected to provide a nuanced understanding of the strengths and weaknesses of each methodological aspect under consideration.

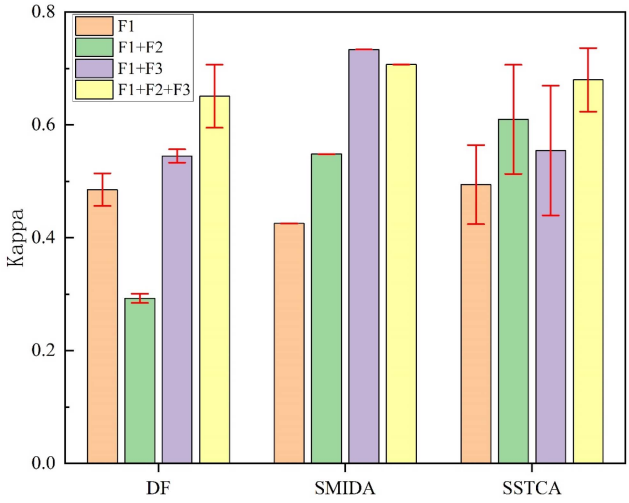

Fig. 9. Grouped bar chart of classification accuracy.

Furthermore, in our detailed analysis of classification results, we utilized additional metrics, including the overall accuracy (OA), *F*-score, Precision, and Recall. OA offers a global view of classification correctness; F-score, as the harmonic mean of Precision and Recall, provides a balanced evaluation, particularly in cases of class imbalance; and Precision reflects the accuracy of classification, while Recall indicates its completeness. The combined use of these metrics allows for a multifaceted evaluation of classification performance, providing a more comprehensive and in-depth analytical foundation.

B. Experimental Results and Analysis

In this comprehensive evaluation, the classification accuracies of the proposed method were scrutinized under varying conditions of labeled sample sizes in the target domain, ranging from 0 to 100. This incremental approach, increasing by a single sample at each step, allowed a nuanced understanding of the models' performance across a continuum from purely transductive transfer learning scenarios (zero target-domain samples) to inductive transfer learning scenarios (one or more target-domain samples).

1) Transductive Transfer Learning Scenario: At zero-labeled samples in the target domain, representing a purely transductive transfer learning scenario, the models relied exclusively on source-domain data. The accuracy of this scenario is crucial as it sets the stage for understanding how well the models can generalize prior to the introduction of any target-domain data. The group bar chart (see Fig. 9) reveals significant insights into the effectiveness of feature selection and the superiority of transfer learning models over the baseline DF model.

The baseline DF model, when enhanced with the VMD features (F3) and the combination of F2 and F3 features, exhibits a significant improvement in accuracy compared with using the F1 feature set alone. This increase indicates that the VMD features can capture more complex and discriminative information from the SAR data. This condition is essential for improving the accuracy of classification without additional labeled data.

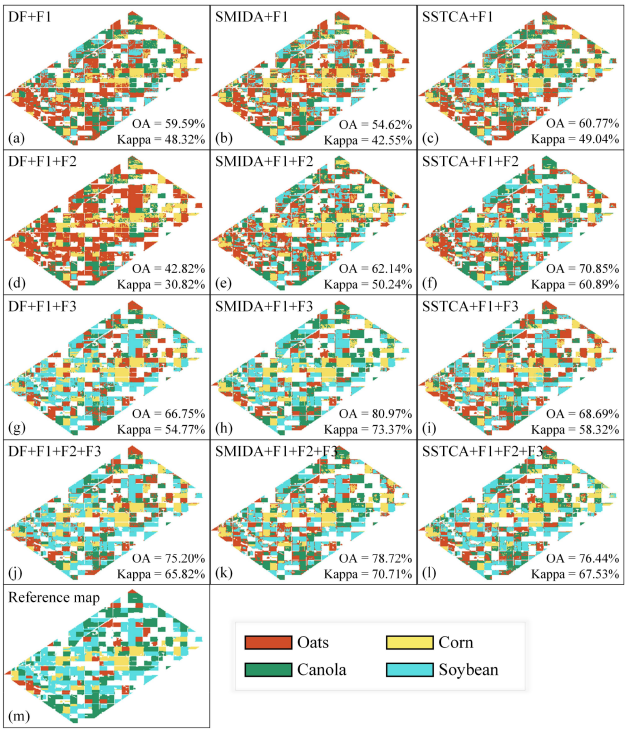

Fig. 10. Classification maps at zero target-domain samples.

TABLE III
ACCURACY STATISTICS AT ZERO TARGET-DOMAIN SAMPLES

Method	F-Score				Precision	Recall	OA	Kappa
	Oats	Canola	Soybean	Corn				
DF+F1	37.20%	81.68%	48.70%	74.89%	71.24%	69.08%	59.59%	48.32%
SMIDA+F1	35.74%	64.35%	52.82%	72.47%	66.59%	65.91%	54.62%	42.55%
SSTCA+F1	39.84%	67.81%	62.21%	76.13%	67.46%	69.94%	60.77%	49.04%
DF+F1+F2	29.92%	73.66%	6.81%	60.91%	65.63%	57.16%	42.82%	30.82%
SMIDA+F1+F2	34.44%	77.09%	63.46%	70.37%	67.12%	66.75%	62.14%	50.24%
SSTCA+F1+F2	44.10%	85.14%	69.59%	78.87%	72.30%	75.47%	70.85%	60.89%
DF+F1+F3	40.03%	50.10%	86.39%	76.47%	65.75%	69.68%	66.75%	54.77%
SMIDA+F1+F3	65.12%	81.51%	88.00%	77.65%	**76.44%**	**82.90%**	**80.97%**	**73.37%**
SSTCA+F1+F3	45.54%	64.95%	82.05%	76.99%	71.75%	74.94%	68.69%	58.32%
DF+F1+F2+F3	52.44%	68.01%	88.95%	78.21%	73.04%	77.99%	75.20%	65.82%
SMIDA+F1+F2+F3	58.12%	82.76%	85.49%	77.44%	**75.70%**	**81.85%**	**78.72%**	**70.71%**
SSTCA+F1+F2+F3	57.82%	74.27%	86.95%	74.83%	**73.03%**	**79.57%**	**76.44%**	**67.53%**

The bold values represent the top 3 results with the highest accuracy.

For the SMIDA model, the introduction of F2, F3, and the combined F2+F3 features leads to a noticeable improvement in classification accuracy compared with the baseline DF model's performance. Similarly, the SSTCA model outperforms the baseline DF model across all feature sets, especially when including F2 and F2+F3 features. This finding indicates that the domain adaptation-based model, with its transfer learning capabilities, can leverage these advanced features more effectively than the baseline model, resulting in better generalization from the source domain.

We then focus our analysis on the corresponding classification maps (see Fig. 10) and accuracy table (see Table III) to further dissect and evaluate the intrinsic merit of incorporating VMD features and its discernible boost to domain adaptation models.

The baseline DF model establishes the foundational performance with an OA of 59.59% and a Kappa coefficient of 48.32%. A significant improvement is achieved with the incorporation of F2 and F3 features, particularly when all feature sets are combined (DF+F1+F2+F3), leading to an OA of 75.20% and a Kappa of 65.82%. This phenomenon highlights the challenges in distinguishing crop types using limited features and the considerable benefit of integrating a comprehensive feature set, especially for soybean classification, the *F*-score of which increased from 48.70% to 88.95%.

The SMIDA model, when augmented with F3 features, demonstrates a notable increase in classification accuracy. The SMIDA+F1+F3 configuration stands out, achieving an OA of 80.97% and a Kappa of 73.37%. This finding is especially significant for oats and canola, where, compared with the baseline (DF+F1+F3), the *F*-scores increase by 25.09% and 31.41%, respectively. Such improvements are particularly meaningful in light of the findings from Section II-B, which indicated that oats and canola share overlapping features, evidenced by their moderate entropy ranges and clustering at alpha angles from 30° to 60°. The pronounced accuracy gain for these crops by SMIDA suggests that the domain adaptation-based approach can effectively enhance the distinctiveness of overlapping feature spaces.

The SSTCA model exhibits robust enhancements with the addition of F2 and F3 features. For example, the SSTCA+F1+F2+F3 configuration achieves an OA of 76.44% and a Kappa of 67.53%. Similar to SMIDA, compared with DF, the SSTCA+F1+F2+F3 configuration shows accuracy improvements mainly for oats and canola, with *F*-scores increasing by 5.38% and 6.26%, respectively. However, a slight reduction in the accuracy for soybean and corn is observed. This finding suggests that while SSTCA refines the feature space discriminability for oats and canola, it could potentially reduce the classification distinction for soybean and corn.

Domain adaptation models were limited in their ability to capture the distributional variances among different crop types under the original HV features, resulting in modest accuracy improvements. To better illustrate the impact of incorporating VMD features, Fig. 11 presents an enlarged view of the near-range area (incidence angle 21.2°–42.2°) from the classification results, as shown in Fig. 10.

As evident from Fig. 11, the introduction of VMD features (F3) has notably elevated the performance of domain adaptation models. The classification results with F3 show improved accuracy and more consistent crop identification, particularly in areas where the original models struggled. This visual comparison clearly demonstrates the significant improvement in classification accuracy brought about by the inclusion of VMD features. This result suggests that VMD features excel in capturing the phenological nuances of crops, thereby significantly refining model efficacy and addressing the subtleties of crop classification challenges.

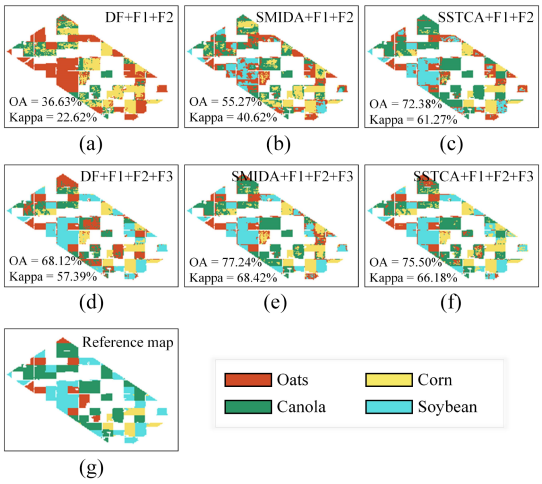

Fig. 11. Enhanced view of classification results in the near-range area (21.2°–42.2° incidence angle) comparing DF, SMIDA, and SSTCA models with and without VMD features (F3).

In summary, the comparative results from the DF, SMIDA, and SSTCA models demonstrate that transfer learning methods can markedly enhance accuracy beyond the baseline model, especially in a transductive learning context without target-domain labeled samples. The efficacy of the VMD-derived features is also validated, given that their inclusion generally leads to significant improvements in classification accuracy, particularly for oats, canola, and soybean. This finding indicates that the temporal characteristics captured by VMD features are especially aligned with the phenological traits of these crops, enhancing their separability in the feature space.

2) Inductive Transfer Learning Scenario: This study also investigates the inductive transfer learning scenario, where a small subset of labeled target-domain samples is integrated. This condition is important for benchmarking the effectiveness of transfer learning models when minimal target-domain data are available. This approach is useful in situations where obtaining extensive labeled data is logistically challenging or costly. The experimental setup is necessary because it can simulate real-world conditions with few samples from the target domain. This method provides important insights into the robustness and practical usefulness of the model.

The accuracy variation of different models, as the number of labeled samples in the target domain increases, is presented in Fig. 12. For the DFATL model, "DFATL+F1+F2+F3+Angle" achieved the highest accuracy in all 20 group results, followed closely by "DFATL+F1+F2+F3." The accuracy curves tend to stabilize when the target-domain sample count reaches around 10, indicating the efficiency of DFATLs active learning approach in selecting the most informative samples. The introduction of the F3 feature set results in a significant increase in accuracy, particularly in the 1–15 target-domain sample range, compared to groups without F3. This emphasizes the advantages of active transfer learning models, which can leverage a small yet informative subset of data to achieve improved accuracy.

When incidence angle information (indicated by "+Angle") is included, the results consistently outperform those of groups without this information. This finding demonstrates the value of incidence angle data in the classification process.

The SMIDA model performs effectively in the transductive setting, but its performance declines slightly in the inductive learning context. Incorporating F3 leads to substantial accuracy gains within the 1–15 sample range, but the gains plateau with larger sample sizes. Interestingly, introducing F2 results in a marked decrease in performance, possibly due to the model's specific characteristics that may not optimally capitalize on the information provided by F2.

The SSTCA model demonstrates minimal improvement with the inclusion of only F3. However, when F2 and F3 are combined, a significant increase in accuracy, particularly within the 1–50 target-domain sample range, is observed. The highest accuracy for SSTCA is achieved with the full feature set (F1+F2+F3).

For the baseline DF model, accuracy incrementally increases with the addition of target-domain samples. This trend signifies the presence of a distribution discrepancy between the initial training and test datasets. This difference diminishes as more samples are introduced, thereby enhancing accuracy. In this scenario, the combination of F1+F2+F3 exhibits the highest accuracy, followed by F1+F3, F1+F2 and then F1 alone. This gradation affirms the contribution of comprehensive feature sets to overcoming distributional inconsistencies caused by incidence angle effects.

Then, transitioning from a broad evaluation of model accuracies across different sizes of target-domain samples, we focus our analysis on the classification results obtained with a target-domain sample size of five. This sample size is selected to further assess the effectiveness of transfer learning, VMD features, and the incorporation of incidence angle information in enhancing classification accuracy. The selection of five samples is deliberate, representing a scenario that is practically relevant and challenging, offering a middle ground, where the benefits of advanced modeling techniques can manifest without requiring extensive labeled data. The results of the DFATL model, an active transfer learning approach, were contrasted with those of the baseline DF model to underscore the nuanced improvements in precision achieved by active learning strategies to the fore in resource-constrained settings. The results in Fig. 13 represent the experiment whose accuracy is nearest to the ten-experiment average. Corresponding *F*-score statistics for each crop type are detailed in Table IV.

At a target-domain sample size of five, the DF model with the *F*1 feature set shows reasonable performance, with an OA of 69.84% and a Kappa of 59.76%. However, when we examine the DFATL model with the same F1 feature set, a noticeable drop of 65.11% and 53.63% in OA and Kappa, respectively, was observed.

Interestingly, the addition of angle information (DFATL+F1+Angle) does not substantially improve the model's accuracy, with OA slightly increasing to 63.94% but Kappa remaining low at 52.84%. This finding suggests that while angle information can be beneficial, its impact is dependent on the model's ability to effectively integrate it into the learning process.

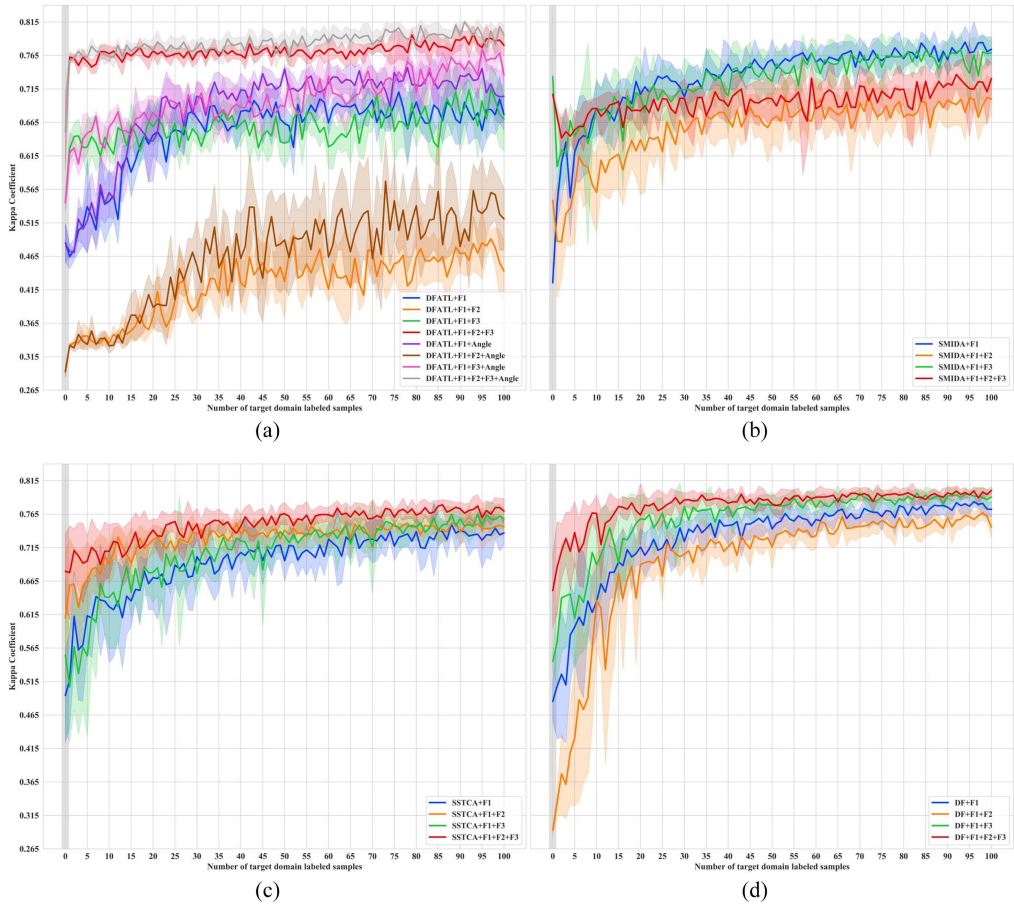

Fig. 12. Variation in the accuracy of different methods with an increasing number of target-domain samples.

TABLE IV
ACCURACY STATISTICS AT FIVE TARGET-DOMAIN SAMPLES

Method	F-Score				Precision	Recall	OA	Kappa
	Oats	Canola	Soybean	Corn				
DF+F1	44.84%	81.28%	74.60%	75.17%	74.33%	74.63%	69.84%	59.76%
DFATL+F1	43.19%	78.50%	63.49%	73.36%	70.88%	70.82%	65.11%	53.63%
DFATL+F1 +Angle	41.04%	80.96%	55.77%	79.59%	71.42%	72.15%	63.94%	52.84%
DF+F1+F2	47.05%	60.89%	88.18%	82.04%	74.34%	76.47%	71.28%	61.31%
DFATL+F1+F2	45.26%	57.00%	86.08%	80.24%	71.99%	74.71%	68.87%	58.30%
DFATL+F1+F2 +Angle	51.04%	71.42%	84.64%	79.74%	73.59%	78.38%	73.54%	64.11%
DF+F1+F2+F3	65.83%	83.75%	86.17%	75.10%	**76.03%**	**82.30%**	**80.71%**	**72.99%**
DFATL+F1+F2 +F3	68.26%	84.13%	88.83%	79.37%	**78.37%**	**83.99%**	**83.02%**	**76.00%**
DFATL+F1+F2 +F3+Angle	68.15%	83.39%	89.78%	80.72%	**78.88%**	**83.89%**	**83.44%**	**76.49%**

The bold values represent the top 3 results with the highest accuracy.

The addition of F2 features, which likely include more detailed temporal information, results in a significant performance enhancement for the DF model (DF+F1+F2), with OA and Kappa increasing to 71.28% and 61.31%. This enhancement is less pronounced in the DFATL model (DFATL+F1+F2) and further boosted when angle information is introduced (DFATL+F1+F2+Angle), suggesting that combining detailed temporal features with angle information could better delineate crop types, reflected in the higher Kappa of 64.11%.

The most notable improvements are observed when combining all feature sets (F1+F2+F3), with the DF model reaching an OA of 80.71% and a Kappa of 72.99%. This improvement is even more pronounced in the DFATL model (DFATL+F1+F2+F3), which achieves an OA of 83.02% and a Kappa of 76.00%. The integration of angle information into this comprehensive feature set (DFATL+F1+F2+F3+Angle) maintains a high level of accuracy, suggesting that the model utilizes the comprehensive features effectively.

These results highlight that even with the addition of a small number of target-domain samples, transfer learning models can leverage the additional information to significantly improve classification accuracy. Evidently, the advanced features, especially when used in conjunction with angle information in the DFATL model, enhance the model's capacity to generalize from a limited sample set. This ability is crucial for practical applications where abundant labeled data may be unavailable.

Several conclusions can be drawn from the synthesis of these experimental outcomes.

1) Notable differences in data distribution are introduced by incidence angle effects. Classification accuracy can be effectively enhanced by introducing transfer learning methods and appropriate feature sets.

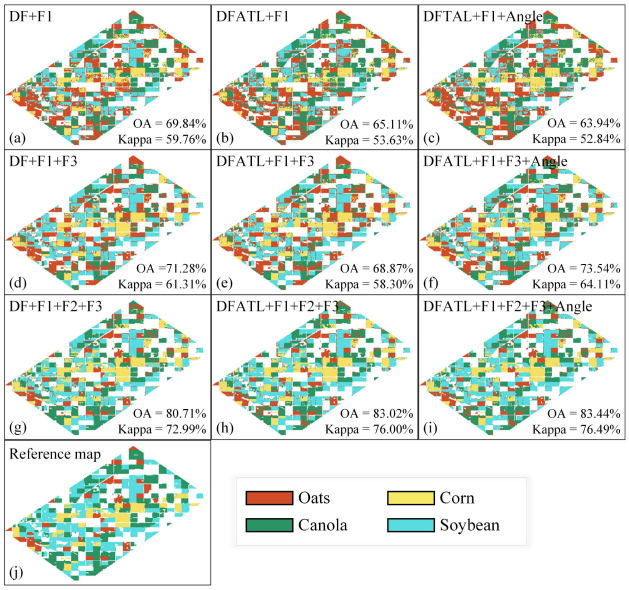

Fig. 13. Classification accuracy map for five labeled samples in the target domain.

2) Different transfer learning models demonstrate varying degrees of suitability for specific scenarios, as illustrated by the distinct performance profiles of DFATL, SMIDA, and SSTCA.
3) The use of features derived from VMD (F3) has shown significant potential in improving model performance, particularly when limited target-domain data are available.
4) The strategy of inclusion incidence angle information in DFATLs model training is effective in refining classification result.

V. Discussion

A. Analysis of the Effectiveness of the Incidence Angle Information Utilization Strategy

A detailed evaluation was conducted to discern the incremental benefits of incorporating incidence angle information within the DFATL model. While the introduction of angle information can enhance accuracy even with a minimal set of target-domain samples, its impact becomes more pronounced as the number of target-domain samples increases. Therefore, we have selected the classification results of DFATL with a target-domain sample size of 100 for this examination to provide a deeper and clearer analysis of how incidence angle information can suppress incidence angle effects and boost classification accuracy.

We adopted the following procedure to analyze the effectiveness of incorporating incidence angle information. For the selected classification results, all image pixels are divided using the incidence angle value, with an interval of 1°. Therefore, the pixels corresponding to each 1° increment of incidence angle are grouped and assessed collectively. The classification accuracy for each angle-based group is computed separately. The resulting accuracies are depicted in Fig. 14, illustrating the varying impacts of incidence angle information across different angle ranges. The corresponding accuracy statistics are presented in Table V.

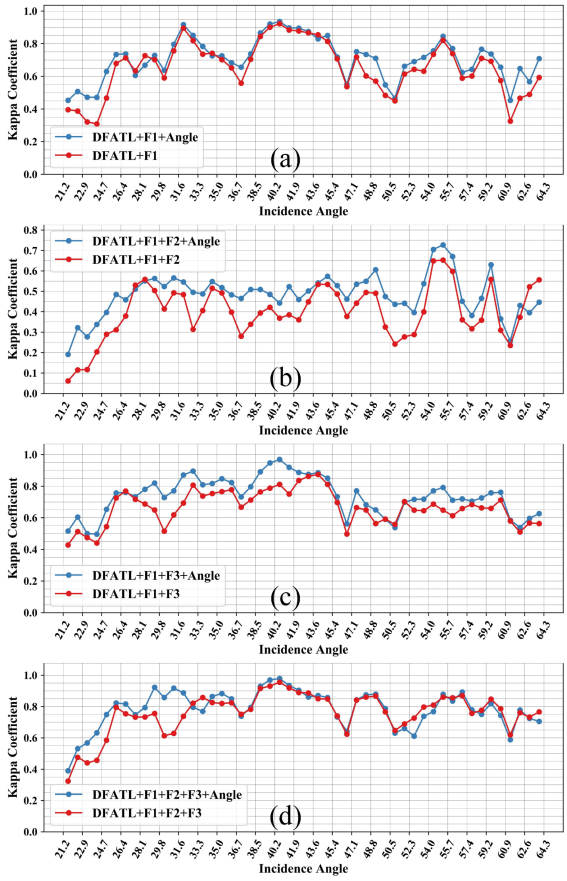

Fig. 14. Classification accuracy of samples in different incidence angle regions.

TABLE V
Accuracy Statistics at 100 Target-Domain Samples

Method	F-Score				Precision	Recall	OA	Kappa
	Oats	Canola	Soybean	Corn				
DFATL+F1	54.93%	85.15%	76.63%	73.20%	74.95%	76.74%	74.91%	65.19%
DFATL+F1 +Angle	63.09%	86.89%	82.32%	74.41%	77.12%	79.94%	79.77%	71.39%
DFATL+F1+F2	35.15%	82.52%	35.42%	70.05%	63.08%	64.52%	55.12%	42.53%
DFATL+F1+F2 +Angle	39.99%	80.85%	55.99%	72.19%	66.76%	69.12%	62.13%	50.16%
DFATL+F1+F3	53.92%	71.92%	88.44%	78.81%	75.16%	76.17%	76.96%	67.30%
DFATL+F1+F3 +Angle	65.48%	81.70%	88.53%	77.61%	**78.98%**	**80.72%**	**81.57%**	**73.61%**
DFATL+F1+F2 +F3	72.31%	85.87%	90.16%	81.99%	**81.83%**	**84.24%**	**85.33%**	**78.85%**
DFATL+F1+F2 +F3+Angle	76.20%	87.92%	88.69%	81.52%	**84.84%**	**82.52%**	**86.12%**	**79.60%**

The bold values represent the top 3 results with the highest accuracy.

For each control group within the DFATL model, an analysis was conducted to initially identify the incidence angle ranges, where the integration of angle information results in enhanced accuracy. Subsequently, potential reasons for these improvements were explored.

Fig. 14(a) clearly illustrates that the classification accuracy for "DFATL+F1+Angle" surpasses that of "DFATL+F1" across

various incidence angle regions. This enhancement is particularly marked within the incidence angle ranges of 21.2°–26.4° and 47.1°–50.5°. In Fig. 14(b), the introduction of angle information results in a notable increase in classification accuracy, specifically within the incidence angle interval of 21.2°–55.7°. This consistent improvement across a broad range of angles indicates the effectiveness of incorporating angle data.

Fig. 14(c) shows that, when comparing "DFATL+F1+F3" to "DFATL+F1+F3+Angle," the introduction of angle information provides a notable improvement in classification accuracy across most incidence angle ranges. The enhancement is especially evident in the range of 21.2°–33.3°, where the accuracy peaks significantly with the addition of angle data. When analyzing "DFATL+F1+F2+F3" against "DFATL+F1+F2+F3+Angle," as shown in Fig. 14(d), we observe that the classification accuracy of the former is relatively low in the incidence angle range of 21.2°–33.3°. Introducing angle information with "DFATL+F1+F2+F3+Angle" significantly enhances classification accuracy within this critical region.

The discernible improvement in classification accuracy within specific incidence angle ranges underscores the substantial contribution of angle information, particularly in areas where the incidence angle effect significantly influences the SAR signal's characteristics. By integrating this geometric information with VMD-derived features, the model effectively mitigates the incidence angle effect, yielding more precise classification outcomes.

A notable observation is that, for the DFATL model, the inclusion of angle information ("+Angle") significantly boosts classification accuracy for oats and soybean. When the F3 feature is added to the F1 set, the accuracy for soybean is improved but that for canola is slightly diminished. With the introduction of F3 into the F1+F2 set, all categories except canola exhibited enhanced classification accuracy. This result is further amplified when F2, F3, and angle information are combined within the F1 set, thereby improving accuracy across all four crop categories. These findings highlight the effectiveness of angle information and the robustness of the F3 feature in the classification process.

The outcomes strongly imply that the incorporation of incidence angle information into the model training is a potent strategy to enhance the model's predictive capabilities, particularly in regions that pose classification challenges. The experimental results validate the proposed training strategy of this study, considering incidence angle information; it significantly improves the classification accuracy across various incidence angle regions. This condition is especially pertinent in areas that traditionally have been more difficult to classify with accuracy.

B. Analysis of the Effectiveness of the VMD

These experiments have confirmed the effectiveness of features derived from VMD in distinguishing different crops. In this section, we aim to delve deeper into the interpretation of these VMD-derived features. We attempt to combine rainfall and crop phenology information to further elucidate the underlying significance of the features extracted from VMD on crop temporal curves across varying incidence angles.

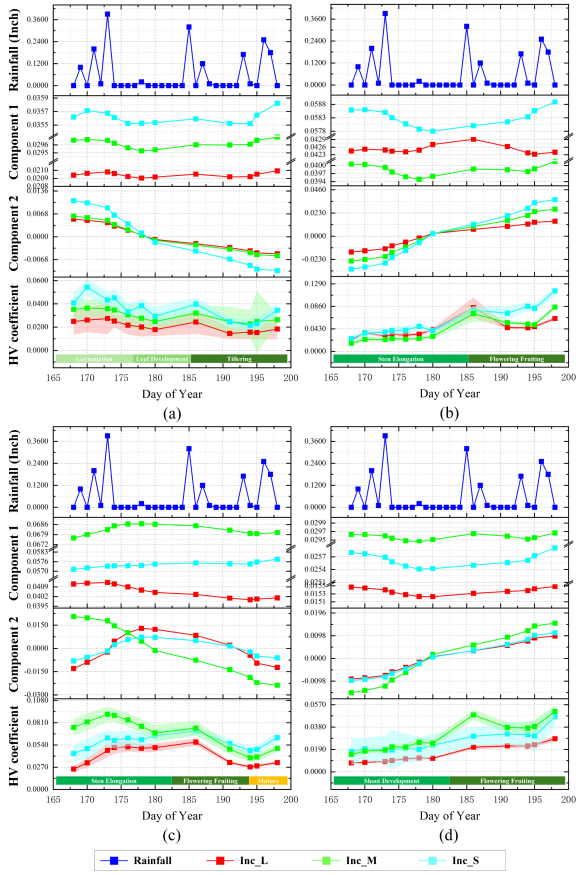

Fig. 15. Schematic of the VMD decomposition results for the HV time series. (a) Oats. (b) Corn. (c) Canola. (d) Soybean.

To achieve this condition, following the methodology of the prior study [10], the image was segmented into three equal regions in accordance with the incidence angles: small (21.2°–32.0°, Inc_S), medium (50.0°–56.0°, Inc_M), and large (60.0°–64.3°, Inc_L). We sampled 100 instances of each crop type from each region, averaged the S_{HV} for each time phase, and constructed temporal curves, achieving 12 curves across the three regions. These curves were then decomposed into two components using VMD, as shown in Fig. 15. The daily precipitation curve during the monitoring period is also displayed in Fig. 15, with data sourced from the National Oceanic and Atmospheric Administration. In addition, the growth period information [47], [48], [49] for each crop type has been annotated in the figure.

Fig. 15 evidently shows that, in the original HV curve, the distinction between certain crops is subtle. For instance, oats and canola exhibit minimal differences from soybean, and some corn can be easily misclassified as canola. Moreover, the similarity of the same crop under different incidence angles is notably low, potentially impacting classification accuracy.

The first component extracted from the VMD primarily reflects changes in soil moisture content. The existing research [16], [50] indicates a significant lag correlation between soil moisture content changes and precipitation. When rainfall occurs, soil moisture content subsequently increases, a trend

reflected in subsequent measurements. This lag effect is attributable to the soil's absorption and retention capabilities. In the VMD decomposition results, the first component of all four crops displays this lag correlation with the precipitation curve, confirming its primary reflection of changes in soil moisture content. Notably, significant differences exist in the first component of the same crop under different incidence angles, probably due to varying responses to changes in soil moisture. These variations for the same crop might reduce the similarity between the same crops in classification, affecting accuracy.

The second component extracted via VMD mainly encapsulates information related to the growth cycle of crops. When compared with the original backscatter coefficient curve, the regularity of the curve of the same crop across different incidence angle regions in the second component is more pronounced, and the numerical differences are significantly reduced. In addition, distinct differences exist between the curves of different crops. This finding suggests that the second component enables a clearer capture of the growth characteristics and periodic changes of crops, thereby enhancing the distinction among different crop types.

As demonstrated in Section IV, the integration of the third feature set (F3), specifically the second component extracted from VMD, into the classification framework markedly enhances accuracy. The enhanced classifier performance, particularly in regions with disparate incidence angles, underscores the use of VMD in mitigating the adverse effects of incidence angle variability on classification. The 12-D VMD decomposition feature, identical to the original feature dimension, not only maintains the complexity of the data but also enhances its interpretability and classification potential.

In summary, the experimental results substantiate that VMD effectively separates soil moisture and growth-related components from the SAR temporal signatures, enhancing crop classification across various incidence angles. Therefore, VMD, which originates from the field of signal processing, has significant potential for enhancing SAR-based agricultural monitoring.

C. Applicability, Extensibility, and Limitations of the Proposed Method

The preceding sections have demonstrated the effectiveness of the proposed method in mitigating the impact of the incidence angle effect on crop classification using airborne SAR data. One of the core innovations of our study is the integration of polarization information, incidence angle data, and the VMD technique through a transfer learning framework to improve the robustness and spatial adaptability of the classifier. This strategy of comprehensively utilizing multiple dimensions of SAR data (polarization, incidence angle, and time) enables a more comprehensive characterization of crop characteristics and enhances classification performance. However, the applicability, extensibility, and limitations of the proposed method must be discussed to provide a comprehensive understanding of its potential and scope.

Regarding the applicability of the method in data-scarce scenarios, although this study utilized a time series of 12 SAR images, the core idea of the method lies in extracting stable crop features and enhancing classifier adaptability through VMD and transfer learning. This conceptual framework remains valid even when the available data are limited. Future research could explore the integration of multisource data and the adoption of few-shot learning techniques to further improve the method's robustness in data-scarce situations.

Concerning the universality of the proposed method across various SAR datasets, including both airborne and spaceborne SAR data, several crucial aspects warrant consideration. Primarily, our approach addresses data distribution disparities without directly accounting for band-specific information, theoretically endowing it with cross-band applicability potential. However, its performance across different bands necessitates validation through future research. Regarding platform differences, airborne and spaceborne SAR systems exhibit significant variations in incidence angle ranges. Airborne SAR typically encompasses a wider range of incidence angles, providing a more challenging testing environment for our method. Given the method's exemplary performance with airborne SAR data, we posit that it may prove even more effective in managing the relatively smaller incidence angle variations characteristic of spaceborne SAR. Nevertheless, it is important to note that spaceborne SAR generally covers larger swaths, potentially leading to greater topographic variations between near and far ranges. This could exacerbate data distribution disparities and increase processing complexity.

Additionally, differing noise levels across platforms may impact the transferability of sample information, constituting another critical factor to consider when applying this method. Spatial resolution differences represent another key consideration. In lower resolution datasets, the presence of mixed pixels may further intensify data distribution disparities, potentially reducing model transferability. Moreover, this could diminish the robustness of the VMD algorithm in extracting regular features of ground objects. Consequently, applying the method to data of varying resolutions may necessitate adjustments to VMD parameters and transfer learning strategies.

While the proposed method has demonstrated promising results, its limitations and potential for broader application must be carefully considered. Future research should focus on several key areas to enhance and validate the method's applicability. This includes validating the method's generalizability across more diverse agricultural landscapes and cropping systems, as well as assessing its efficacy across different bands, platforms, and resolutions of SAR data. Such assessment is particularly important, given the potential impacts of varying incidence angle ranges, spatial resolutions, and noise levels characteristic of different SAR systems. Additionally, exploring optimizations to accommodate these variations will be crucial, potentially involving fine-tuning VMD parameters, enhancing transfer learning strategies, and developing new techniques to handle mixed pixels that are more prevalent in lower resolution data. By addressing these aspects, future studies cannot only validate the method's broader applicability but also potentially extend its capabilities to handle a wider range of SAR data types.

VI. Conclusion

In this study, we introduced a comprehensive framework that synergistically combines transfer learning, VMD, and incidence angle information to effectively address the impact of incidence angle effects on airborne SAR time-series image classification. The proposed method exhibits improved performance in classifying crops across the full incidence angle range compared with the existing techniques. Our main findings are as follows.

1) Transfer learning can effectively manage data distribution discrepancies arising from diverse incidence angles, enhancing the model's adaptability and robustness.
2) VMD can isolate components and enable a clearer capture of the growth characteristics and periodic changes of crops, improving the discrimination among different crop types.
3) Incidence angle information can serve as important auxiliary data to improve the model's performance.

The innovative integration of interdisciplinary technologies from different fields not only provides new perspectives for overcoming this specific challenge but also serves as an important reference for solving various problems in areas, such as land-use change detection and disaster assessment within time-series SAR-based studies. Future studies must focus on using more real-world data for testing to further validate and refine our approach.

Acknowledgment

The authors would like to thank the JPL NASA and SMAPVEX 2012 teams for providing the UAVSAR images, and the NASA National Snow and Ice Data Center Distributed Active Archive Center (NSIDC DAAC) for making and providing the 2012 crop map of the Winnipeg area.

References

[1] T. W. Hertel, "The challenges of sustainably feeding a growing planet," *Food Secur.*, vol. 7, no. 2, pp. 185–198, Apr. 2015, doi: 10.1007/s12571-015-0440-2.

[2] B. Wu et al., "Challenges and opportunities in remote sensing-based crop monitoring: A review," *Nat. Sci. Rev.*, vol. 10, Apr. 2023, Art. no. nwac290, doi: 10.1093/nsr/nwac290.

[3] B. Wu et al., "Global crop monitoring: A satellite-based hierarchical approach," *Remote Sens.*, vol. 7, no. 4, pp. 3907–3933, Apr. 2015, doi: 10.3390/rs70403907.

[4] S. Fritz et al., "Mapping global cropland and field size," *Glob. Change Biol.*, vol. 21, no. 5, pp. 1980–1992, 2015, doi: 10.1111/gcb.12838.

[5] M. E. Qureshi, J. Dixon, and M. Wood, "Public policies for improving food and nutrition security at different scales," *Food Secur.*, vol. 7, no. 2, pp. 393–403, Apr. 2015, doi: 10.1007/s12571-015-0443-z.

[6] C. F. Nicholson, E. C. Stephens, B. Kopainsky, A. D. Jones, D. Parsons, and J. Garrett, "Food security outcomes in agricultural systems models: Current status and recommended improvements," *Agricultural Syst.*, vol. 188, Mar. 2021, Art. no. 103028, doi: 10.1016/j.agsy.2020.103028.

[7] F. Canisius et al., "Tracking crop phenological development using multitemporal polarimetric radarsat-2 data," *Remote Sens. Environ.*, vol. 210, pp. 508–518, Jun. 2018, doi: 10.1016/j.rse.2017.07.031.

[8] G. W. Gella, W. Bijker, and M. Belgiu, "Mapping crop types in complex farming areas using SAR imagery with dynamic time warping," *ISPRS J. Photogramm. Remote Sens.*, vol. 175, pp. 171–183, May 2021, doi: 10.1016/j.isprsjprs.2021.03.004.

[9] N. Bhogapurapu et al., "Dual-polarimetric descriptors from Sentinel-1 GRD SAR data for crop growth assessment," *ISPRS J. Photogramm. Remote Sens.*, vol. 178, pp. 20–35, Aug. 2021, doi: 10.1016/j.isprsjprs.2021.05.013.

[10] X. Qin et al., "Active pairwise constraint learning in constrained time-series clustering for crop mapping from Airborne SAR imagery," *Remote Sens.*, vol. 14, no. 23, Nov. 2022, Art. no. 6073, doi: 10.3390/rs14236073.

[11] D. Mandal et al., "Dual polarimetric radar vegetation index for crop growth monitoring using sentinel-1 SAR data," *Remote Sens. Environ.*, vol. 247, Sep. 2020, Art. no. 111954, doi: 10.1016/j.rse.2020.111954.

[12] H. Shi et al., "Soil moisture estimation using two-component decomposition and a hybrid X-Bragg/Fresnel scattering model," *J. Hydrol.*, vol. 574, pp. 646–659, Jul. 2019, doi: 10.1016/j.jhydrol.2019.04.049.

[13] C. H. Menges, J. J. Van Zyl, G. J. E. Hill, and W. Ahmad, "A procedure for the correction of the effect of variation in incidence angle on AIR-SAR data," *Int. J. Remote Sens.*, vol. 22, no. 5, pp. 829–841, Jan. 2001, doi: 10.1080/01431160051060264.

[14] I. E. Mladenova, T. J. Jackson, R. Bindlish, and S. Hensley, "Incidence angle normalization of radar backscatter data," *IEEE Trans. Geosci. Remote Sens.*, vol. 51, no. 3, pp. 1791–1804, Mar. 2013, doi: 10.1109/TGRS.2012.2205264.

[15] H. Tamiminia, S. Homayouni, H. McNairn, and A. Safari, "A particle swarm optimized kernel-based clustering method for crop mapping from multi-temporal polarimetric L-band SAR observations," *Int. J. Appl. Earth Observ. Geoinf.*, vol. 58, pp. 201–212, Jun. 2017, doi: 10.1016/j.jag.2017.02.010.

[16] H. McNairn et al., "The soil moisture active passive validation experiment 2012 (SMAPVEX12): Prelaunch calibration and validation of the SMAP soil moisture algorithms," *IEEE Trans. Geosci. Remote Sens.*, vol. 53, no. 5, pp. 2784–2801, May 2015, doi: 10.1109/TGRS.2014.2364913.

[17] I. Khosravi and S. K. Alavipanah, "A random forest-based framework for crop mapping using temporal, spectral, textural and polarimetric observations," *Int. J. Remote Sens.*, vol. 40, no. 18, pp. 7221–7251, Sep. 2019, doi: 10.1080/01431161.2019.1601285.

[18] W. Wagner, J. Noll, M. Borgeaud, and H. Rott, "Monitoring soil moisture over the Canadian Prairies with the ERS scatterometer," *IEEE Trans. Geosci. Remote Sens.*, vol. 37, no. 1, pp. 206–216, Jan. 1999, doi: 10.1109/36.739155.

[19] J. P. Ardila, V. Tolpekin, and W. Bijker, "Angular backscatter variation in L-band ALOS ScanSAR images of tropical forest areas," *IEEE Geosci. Remote Sens. Lett.*, vol. 7, no. 4, pp. 821–825, Oct. 2010, doi: 10.1109/LGRS.2010.2048411.

[20] K. Weiss, T. M. Khoshgoftaar, and D. Wang, "A survey of transfer learning," *J. Big Data*, vol. 3, no. 1, Dec. 2016, Art. no. 9, doi: 10.1186/s40537-016-0043-6.

[21] S. J. Pan and Q. Yang, "A survey on transfer learning," *IEEE Trans. Knowl. Data Eng.*, vol. 22, no. 10, pp. 1345–1359, Oct. 2010, doi: 10.1109/TKDE.2009.191.

[22] K. Dragomiretskiy and D. Zosso, "Variational mode decomposition," *IEEE Trans. Signal Process.*, vol. 62, no. 3, pp. 531–544, Feb. 2014, doi: 10.1109/TSP.2013.2288675.

[23] V. R. Carvalho, M. F. D. Moraes, A. P. Braga, and E. M. A. M. Mendes, "Evaluating five different adaptive decomposition methods for EEG signal seizure detection and classification," *Biomed. Signal Process. Control*, vol. 62, Sep. 2020, Art. no. 102073, doi: 10.1016/j.bspc.2020.102073.

[24] H. McNairn, J. Powers, and G. Wiseman, "SMAPVEX12 land cover classification map, version 1. [June to July 2012]," NASA Nat. Snow Ice Data Center Distrib. Active Archive Center, Boulder, CO USA, 2014.

[25] T. Shibayama, Y. Yamaguchi, and H. Yamada, "Polarimetric scattering properties of landslides in forested areas and the dependence on the local incidence angle," *Remote Sens.*, vol. 7, no. 11, pp. 15424–15442, Nov. 2015, doi: 10.3390/rs71115424.

[26] L. Zhao, J. Yang, P. Li, and L. Zhang, "Seasonal inundation monitoring and vegetation pattern mapping of the Erguna floodplain by means of a RADARSAT-2 fully polarimetric time series," *Remote Sens. Environ.*, vol. 152, pp. 426–440, 2014, doi: 10.1016/j.rse.2014.06.026.

[27] T. Whelen and P. Siqueira, "Use of time-series L-band UAVSAR data for the classification of agricultural fields in the San Joaquin Valley," *Remote Sens. Environ.*, vol. 193, pp. 216–224, May 2017, doi: 10.1016/j.rse.2017.03.014.

[28] X. Huang et al., "Cropland mapping with L-band UAVSAR and development of NISAR products," *Remote Sens. Environ.*, vol. 253, 2021, Art. no. 112180, doi: 10.1016/j.rse.2020.112180.

[29] J.-E. Ouzemou et al., "Crop type mapping from pansharpened Landsat 8 NDVI data: A case of a highly fragmented and intensive agricultural system," *Remote Sens. Appl., Soc. Environ.*, vol. 11, pp. 94–103, 2018, doi: 10.1016/J.RSASE.2018.05.002.

[30] Y. Kang et al., "Land cover and crop classification based on red edge indices features of GF-6 WFV time series data," *Remote. Sens.*, vol. 13, 2021, Art. no. 4522, doi: 10.3390/rs13224522.
[31] Z. H. Zhou and J. Feng, "Deep forest, *Nat. Sci. Rev.*, vol. 6, no 1, pp. 74–86, Jan. 2019, doi: 10.1093/nsr/nwy108.
[32] M. Fernandez-Delgado, E. Cernadas, S. Barro, and D. Amorim, "Do we need hundreds of classifiers to solve real world classification problems?," *J. Mach. Learn. Res.*, vol. 15, pp. 3133–3181, Oct. 2014.
[33] S. Piao et al., "Summer soil moisture regulated by precipitation frequency in China," *Environ. Res. Lett.*, vol. 4, 2009, Art. no. 044012, doi: 10.1088/1748-9326/4/4/044012.
[34] X. Huang, Z. Shi, H. Zhu, H. Zhang, L. Ai, and W. Yin, "Soil moisture dynamics within soil profiles and associated environmental controls," *Catena*, vol. 136, pp. 189–196, 2016, doi: 10.1016/J.CATENA.2015.01.014.
[35] Y. Yang, X. Dong, Z. Peng, W. Zhang, and G. Meng, "Component extraction for non-stationary multi-component signal using parameterized de-chirping and band-pass filter," *IEEE Signal Process. Lett.*, vol. 22, no. 9, pp. 1373–1377, Sep. 2015, doi: 10.1109/LSP.2014.2377038.
[36] H. Li, B. Fan, R. Jia, F. Zhai, L. Bai, and X. Luo, "Research on multi-domain fault diagnosis of gearbox of wind turbine based on adaptive variational mode decomposition and extreme learning machine algorithms," *Energies*, vol. 13, 2020, Art. no. 1375, doi: 10.3390/en13061375.
[37] G. Tang and X. Wang, "Variational mode decomposition method and its application on incipient fault diagnosis of rolling bearing," *J. Vib. Eng.*, vol. 29, no. 4, pp. 638–648, 2016, doi: 10.16385/j.cnki.issn.1004-4523.2016.04.011.
[38] R. M. Haralick, K. Shanmugam, and I. Dinstein, "Textural features for image classification," *IEEE Trans. Syst., Man, Cybern.*, vol. SMC-3, no. 6, pp. 610–621, Nov. 1973, doi: 10.1109/TSMC.1973.4309314.
[39] D. Jia, P. Gao, C. Cheng, and S. Ye, "Multiple-feature-driven co-training method for crop mapping based on remote sensing time series imagery," *Int. J. Remote Sens.*, vol. 41, no. 20, pp. 8096–8120, Oct. 2020, doi: 10.1080/01431161.2020.1771790.
[40] C. Deng, Y. Xue, X. Liu, C. Li, and D. Tao, "Active transfer learning network: A unified deep joint spectral–spatial feature learning model for hyperspectral image classification," *IEEE Trans. Geosci. Remote Sens.*, vol. 57, no. 3, pp. 1741–1754, Mar. 2019, doi: 10.1109/TGRS.2018.2868851.
[41] X. Liu, G. Wang, Z. Cai, and H. Zhang, "Bagging based ensemble transfer learning," *J Ambient Intell. Humanized Comput.*, vol. 7, no. 1, pp. 29–36, Feb. 2016, doi: 10.1007/s12652-015-0296-5.
[42] X. Qin, J. Yang, L. Zhao, P. Li, and K. Sun, "A novel deep forest-based active transfer learning method for PolSAR images," *Remote Sens.*, vol. 12, no. 17, 2020, Art. no. 2755, doi: 10.3390/rs12172755.
[43] K. Yan, L. Kou, and D. Zhang, "Learning domain-invariant subspace using domain features and independence maximization," *IEEE Trans. Cybern.*, vol. 48, no. 1, pp. 288–299, Jan. 2018, doi: 10.1109/TCYB.2016.2633306.
[44] S. J. Pan, I. W. Tsang, J. T. Kwok, and Q. Yang, "Domain adaptation via transfer component analysis," *IEEE Trans. Neural Netw.*, vol. 22, no. 2, pp. 199–210, Feb. 2011, doi: 10.1109/TNN.2010.2091281.
[45] K. M. Borgwardt, A. Gretton, M. J. Rasch, H.-P. Kriegel, B. Scholkopf, and A. J. Smola, "Integrating structured biological data by kernel maximum mean discrepancy," *Bioinformatics*, vol. 22, no. 14, pp. e49–e57, Jul. 2006, doi: 10.1093/bioinformatics/btl242.
[46] A. I. Schein and L. H. Ungar, "Active learning for logistic regression: An evaluation," *Mach. Learn.*, vol. 68, no. 3, pp. 235–265, Aug. 2007, doi: 10.1007/s10994-007-5019-5.
[47] N. W. W. Ort, M. J. Morrison, E. R. Cober, D. McAndrew, and Y. E. Lawley, "A comparison of soybean maturity groups for phenology, seed yield, and seed quality components between eastern Ontario and southern Manitoba," *Can. J. Plant Sci.*, vol. 102, no. 4, pp. 812–822, Aug. 2022, doi: 10.1139/cjps-2021-0235.
[48] "SMAPVEX12," SMAP, Accessed on: Dec. 26, 2023. [Online]. Available: https://smap.jpl.nasa.gov/science/validation/fieldcampaigns/SMAPVEX12
[49] H. Wang, R. Magagi, and K. Goita, "Polarimetric decomposition for monitoring crop growth status," *IEEE Geosci. Remote Sens. Lett.*, vol. 13, no. 6, pp. 870–874, Jun. 2016, doi: 10.1109/LGRS.2016.2551377.
[50] H. Wang, R. Magagi, and K. Goita, "Comparison of different polarimetric decompositions for soil moisture retrieval over vegetation covered agricultural area," *Remote Sens. Environ.*, vol. 199, pp. 120–136, Sep. 2017, doi: 10.1016/j.rse.2017.07.008.

Xingli Qin received the B.S. degree in remote sensing science and technology from the School of Remote Sensing and Information Engineering, Wuhan University, Wuhan, China, in 2015, and the M.S. degree in surveying and mapping engineering and the Ph.D. degree in photogrammetry and remote sensing from the State Key Laboratory of Information Engineering in Surveying, Mapping, and Remote Sensing, Wuhan University, in 2017 and 2021, respectively.

He is currently an Assistant Researcher with the Key Laboratory of Remote Sensing and Digital Earth, Aerospace Information Research Institute, Chinese Academy of Sciences, Beijing, China. He is also a member of the Global Agricultural Remote Sensing Monitoring Team (CropWatch) of China. His research interests include intelligent interpretation of remote sensing imagery, transfer learning, and agricultural remote sensing. His work combines advanced machine learning techniques with remote sensing data to develop innovative solutions for environmental monitoring and agricultural management.

Lingli Zhao (Member, IEEE) received the B.S. degree in geographic information system from Zhengzhou University, Zhengzhou, China, in 2010, and the Ph.D. degree in photogrammetry and remote sensing from Wuhan University, Wuhan, China, in 2015.

She was a Xiangjiang Scholar with the Department of Land Surveying and Geo-Informatics, The Hong Kong Polytechnic University, Hong Kong, from 2017 to 2019. She has been a Research Fellow with the School of Remote Sensing and Information Engineering, Wuhan University, since 2015. Her research interests include polarimetric SAR image processing and its applications in agriculture, wetland, and disaster monitoring.

Jie Yang received the Ph.D. degree in photogrammetry and remote sensing from Wuhan University, Wuhan, China, in 2004.

Since 2011, he has been a Professor with the State Key Laboratory of Information Engineering in Surveying, Mapping, and Remote Sensing, Wuhan University. His main current research interests include understanding synthetic aperture radar images.

Pingxiang Li received the Ph.D. degree in photogrammetry and remote sensing from Wuhan University, Wuhan, China, in 2003.

Since 2002, he has been a Research Fellow with the State Key Laboratory of Information Engineering in Surveying, Mapping, and Remote Sensing, Wuhan University. His research interests include synthetic aperture radar image processing and applications.

Hongwei Zeng received the Ph.D. degree in natural resources from the Graduate School of the Chinese Academy of Sciences, Beijing, China, in 2012.

He is an Associate Professor with the Key Laboratory of Remote Sensing and Digital Earth, Aerospace Information Research Institute, Chinese Academy of Sciences. He is a member of the Global Agricultural Remote Sensing Monitoring Team (CropWatch) of China and a member of the Executive Committee of the Global Earth Observation Global Agricultural Monitoring Flagship. His research interests include remote sensing identification of crop types, remote sensing estimation methods for crop yields, and comprehensive evaluation of water resources availability at the basin scale driven by machine learning.

Miao Zhang received the Ph.D. degree in cartography and geographical information system from the University of Chinese Academy of Sciences, Beijing, China, in 2014.

He is an Associate Professor with the Key Laboratory of Remote Sensing and Digital Earth, Aerospace Information Research Institute, Chinese Academy of Sciences, Beijing, China. He was a key member of the CropWatch Team, which provides remote-sensing-based global agricultural monitoring through a cloud platform. As a member of the Executive Committee of the GEOGLAM Flagship and a co-lead of the Joint Experiments for Crop Assessment and Monitoring Initiative, he has collaborated with researchers from more than 20 countries and various international organizations within the GEOGLAM framework. His research focuses on remote-sensing-based agriculture monitoring, specifically crop classification using multisource remote sensing imagery and crop area estimates, remote-sensing-based agricultural monitoring and food security assessment, and big Earth data for cropland and cropping intensity mapping.

Kaimin Sun (Member, IEEE) received the B.S., M.S., and Ph.D. degrees in photogrammetry and remote sensing from Wuhan University, Wuhan, China, in 1999, 2004, and 2008, respectively.

He is currently a Professor with the State Key Laboratory of Information Engineering in Surveying, Mapping, and Remote Sensing, Wuhan University. His research interests include photogrammetry, applications of remote sensing in ecology and surface disaster, and time-series analysis of remote sensing images.